Article:
de Borst, R. orcid.org/0000-0002-3457-3574 and Chen, L. (2024) Phase-field modelling of cohesive interface failure. International Journal for Numerical Methods in Engineering, 125 (9). e7412. ISSN 0029-5981

https://doi.org/10.1002/nme.7412

Received: 8 September 2023 | Revised: 28 November 2023 | Accepted: 1 December 2023

DOI: 10.1002/nme.7412

RESEARCH ARTICLE

WILEY

Phase-field modelling of cohesive interface failure

R. de Borst[1] | **L. Chen**[2]

[1]Department of Civil and Structural Engineering, University of Sheffield, Sheffield, UK

[2]Key Laboratory of Ministry of Education on Safe Mining of Deep Metal Mines, Northeastern University, Shenyang, China

Correspondence
R. de Borst, University of Sheffield, Department of Civil and Structural Engineering, Sheffield S1 3JD, UK.
Email: r.deborst@sheffield.ac.uk

Abstract

A cohesive interface model is proposed in the framework of the phase-field approach. The discrete interface is transformed into a smeared interface by a regularisation strategy. Nevertheless, the fracture energy is made dependent on the displacement jump, which is approximated by a first-order Taylor expansion of the displacement at the interface. Its value relies on a proper choice of the distance parameter from the interface. We have derived an optimal distance parameter from the analytical solution of a uniaxial tension problem. The accuracy of the approach for cohesive interface modelling is validated in a one-dimensional numerical test and is demonstrated by two examples, including a 'H'-shaped plate and a fibre embedded in an epoxy matrix, featuring straight and curved interfaces.

KEYWORDS

cohesive zone model, displacement jump, interface, optimal distance parameter, phase field model

1 | INTRODUCTION

The design of structural materials like concrete or composites typically involves several components at the material level or at the structural level, such as fibres, grains and matrix material. In such materials, interface damage may occur, which influences the structural properties of materials and structures. For example, the strength of concrete largely relies on the properties of the mortar-aggregate interface.[1]

Many numerical methods have been developed to investigate interface damage. Starting from the early works in 1960s ,[2,3] two different approaches have been developed for modelling of interfacial failure, namely discrete and smeared models.[4] The discrete approach treats the interface as geometric discontinuities, with tractions on the interface boundaries.[5–10] The smeared method avoids topological changes of the computational domain, distributes the discontinuities over a finite band, for example, References 11–13. After the early works, the smeared approach has been cast in a damage format, while more recently, the phase-field method has been proposed to regularise the interface in a smeared sense.[14–16]

The phase-field approach to fracture finds its origins in the so-called variational approach to fracture.[17] Herein, crack initiation and quasi-static propagation were considered as a minimisation problem of a Griffith-like energy functional. To make the problem amenable to large-scale computations a regularisation strategy was developed subsequently, which transforms the sharp crack into a distributed crack, which is governed by a phase-field variable d. The width of the distributed crack is set by an internal length scale ℓ.[15]

The vast majority of phase-field models have been applied to the analysis of brittle fracture, for example, References 15 and 18. Nevertheless, many natural and man-made materials hold a cohesive property owing to their internal structure, for instance fibre-reinforced composite materials. The phase-field modelling of cohesive fractures in those materials is

not yet well developed. Verhoosel and de Borst[19] regularised the phase-field model[20] to cast the cohesive interface in a smeared format. They employed an auxiliary field to model the displacement jump, which is an essential input of the cohesive-zone model.[21–23] However, the auxiliary field needs to be prescribed in the whole domain, reducing the computational efficiency.[24]

To avoid the introduction of an auxiliary field, Nguyen et al.[25] have computed the displacement jump at two points near the interface. However, the choice of the location of these points suffers from a certain arbitrariness. In the framework of brittle fracture modelling, one can also change the degradation function and the homogeneous energy dissipation function.[18,26–28] As a result, the cohesive relation is reproduced in a one-dimensional setting. Another approach to obtain the displacement jump in brittle phase-field models is to use a line integral to compute the value in the direction normal to the crack.[29,30] Chukwudozie et al.,[31] Yoshioka et al.[32] and Chen et al.[30] have theoretically proven this integral formula, and have detailed the implementation of the integral form. In the brittle fracture model the cohesive interface debonding and the cracking in the bulk can also be considered separately. Then, the cracking in the bulk is described by a brittle model, while the interface behaviour is modelled by the cohesive model.[33–38]

The cohesive phase-field model of Verhoosel and de Borst[19] and Nguyen et al.[25] uses the phase-field regularisation technology to transform a discrete interface into a smeared one. The cohesive law is incorporated in a displacement jump-dependent fracture energy function. This model is elegant, and in general, a powerful approach to implement the cohesive interface within the context of phase-field modelling. It combines the discrete interface model with the smeared approach. The regularisation technology from the phase-field model treats the discrete interface in a smeared sense. The cohesive-zone law from the discrete model is however directly used to describe the interface behaviour. Due to the use of the smeared interface, there is no need to introduce geometric discontinuities in the domain, and it is, for instance, not necessary to introduce enrichment functions like in the extended finite element method (XFEM). The incorporation of the cohesive law in the model is straightforward and directly incorporates the correct physics, which is different from the modification of the degradation function.[18] Moreover, we can consider any form of the cohesive relation, while with the modification of the degradation function only a specific form of the cohesive relation seems to be possible.[18] While so far only an exponential degradation function has been considered by Verhoosel and de Borst[19] and Nguyen et al.,[25] any other degradation function can be incorporated.

This study will address the general case of a phase-field regularised interface cohesive-zone model. We will focus on the elaboration of the localised property of the model, the smeared displacement jump computation, and the derivation of the optimal distance parameter. We will start this contribution with a concise description of regularised cohesive-zone models and phase-field representations of cohesive interfaces. Subsequently, we will elaborate on the smeared representation of discontinuities and the localised property of the smeared interface. Section 4 will focus on the introduction of smeared displacement jump and the derivation of the optimal distance parameter for the jump computation. The finite element implementation is discussed in Section 5. Finally, numerical examples are presented to validate the approach and conclusions are drawn.

2 | PHASE-FIELD MODEL FOR COHESIVE FRACTURE

We consider a domain Ω with an internal interface Γ_i between phases (matrix and inclusions), see Figure 1A. The interface behaviour is described by a cohesive-zone model.[39,40] In the current study, we assume the interface Γ_i to be zero-thickness and pre-defined, as is the case, for instance, for the delamination of composite structures.

2.1 | Energy functional

Introduced in References 39 and 40, cohesive-zone model is now widely used to model interface failure.[41] Cohesive tractions $\mathbf{t}$ on a crack interface are linked to the displacement jump at the interface. The interface Γ_i is placed in the physical domain Ω with positive and negative sides, Γ_i^+ and Γ_i^- respectively, as illustrated in Figure 1A. The cohesive-zone model was originally conceived as a discrete fracture model,[42] with the crack interface being a geometric discontinuity. The fracture energy is then given as:

$$\mathcal{E}_i(\Gamma_i) = \int_{\Gamma_i} \mathcal{G}(\llbracket \mathbf{u} \rrbracket,\ \boldsymbol{\kappa}) \mathrm{d}A \tag{1}$$

with $\boldsymbol{\kappa}$ being a history parameter, and obeying the Kuhn–Tucker conditions to distinguish between loading and unloading. $\mathcal{G}(\llbracket\mathbf{u}\rrbracket,\ \boldsymbol{\kappa})$ is the fracture energy function, defining the energy dissipation upon the creation of a unit crack surface. It is released gradually, and depends on the displacement jump $\llbracket\mathbf{u}\rrbracket$ and the history parameter $\boldsymbol{\kappa}$. The displacement jump $\llbracket\mathbf{u}\rrbracket$ across Γ_i is expressed as

$$\llbracket\mathbf{u}\rrbracket = \mathbf{u}^+ - \mathbf{u}^- \qquad \text{on} \qquad \Gamma_i \tag{2}$$

with $\mathbf{u}^+$ and $\mathbf{u}^-$ being the displacement on the positive and negative sides, Γ_i^+ and Γ_i^- in Figure 1A, respectively.

The cohesive interface Γ_i can be regularised by the phase-field method,[19,25] and represented as a smeared interfaces, see Figure 1B. In Equation (1), the infinitesimal surface area $\mathrm{d}A$, at a point $\mathbf{x}_i$ on the interface Γ_i is then rewritten in an integral form

$$\mathrm{d}A(\mathbf{x}_c) = \underbrace{\int_{x_n=-\infty}^{\infty} \delta(x_n)\mathrm{d}x_n}_{=1}\mathrm{d}A = \int_{x_n=-\infty}^{\infty} \delta(x_n)\mathrm{d}V \approx \int_{x_n=-\infty}^{\infty} \delta_c(x_n)\mathrm{d}V \tag{3}$$

in which $x_n = (\mathbf{x}-\mathbf{x}_i)\cdot\boldsymbol{n}(\mathbf{x}_i)$ and $\boldsymbol{n}(\mathbf{x}_i)$ the unit vector normal to the interface Γ_i. $\delta(x_n)$ represents the Dirac-delta function, being zero everywhere except at x_n. In the numerical implementation one cannot directly use $\delta(x_n)$ to regularise the interface. An approximated form, $\delta_c(x_n)$, must be used instead, that is, the last term in Equation (3). Herein, we will use the phase-field model to obtain $\delta_c(x_n)$. The basic idea is to approximate the discrete interface Γ_i by a smeared interface Γ_i^ξ, as shown in Figure 1B. The explicit form of $\delta_c(x_n)$ will be detailed in Section 3.

Substituting Equation (3) into Equation (1) leads to a phase-field regularised energy function for cohesive fracture[19]:

$$\mathcal{E}_i = \int_{\Gamma_i} \mathcal{G}(\llbracket\mathbf{u}\rrbracket,\ \boldsymbol{\kappa}) \int_{x_n=-\infty}^{\infty} \delta(x_n)\mathrm{d}V \approx \int_{\Omega} \mathcal{G}(\llbracket\mathbf{u}\rrbracket,\ \boldsymbol{\kappa})\delta_c(x_n)\mathrm{d}V. \tag{4}$$

In the course of the loading process cracks can initiate in the solid and propagate into the bulk material, see Figure 1A. The crack initiation and propagation is governed by brittle fracture models.[25,33,43–46] In such a scenario, the cracking in the bulk should be considered in the modelling. In the current study, the focus is on the phase-field representation of the interface, the smeared form of the displacement jump, and the derivation of the optimal distance parameter.

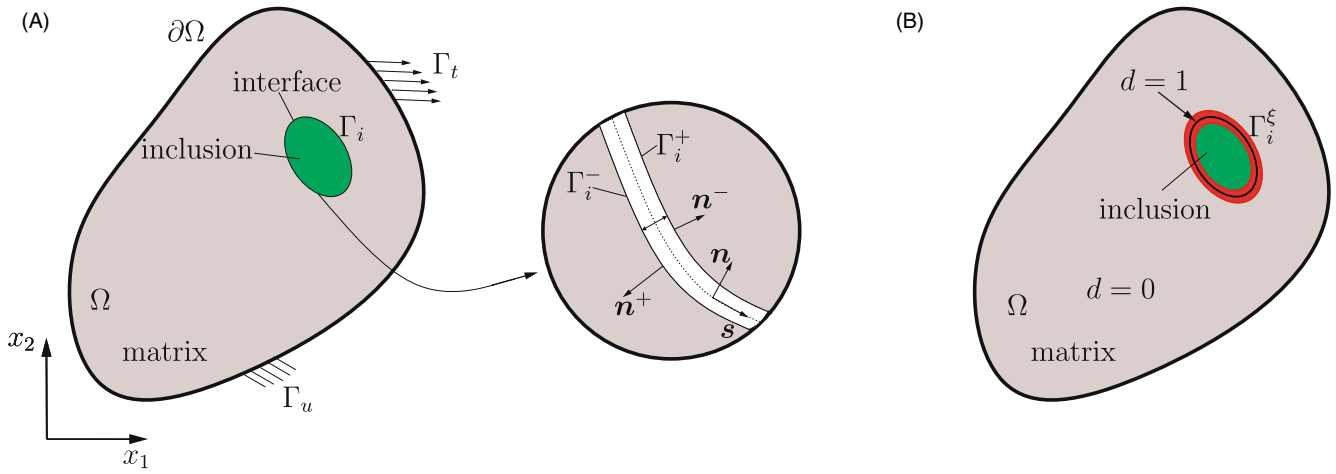

FIGURE 1 (A) A solid body Ω with a discrete interface Γ_i. The latter is represented as overlapping positive and negative sides, Γ_i^+ and Γ_i^-, respectively. Boundary Γ_u is prescribed with a displacement $\bar{\mathbf{u}}$; Γ_t with a prescribed traction $\hat{\mathbf{t}}$. (B) Smeared representation of Γ_i as a smeared interface Γ_i^ξ (red area).

The potential energy of the solid is given as[25]:

$$\Psi_{\text{pot}} = \int_{\Omega} \psi^e(\boldsymbol{\varepsilon}(\mathbf{u}))\mathrm{d}V + \int_{\Gamma_i} \mathcal{G}(\llbracket \mathbf{u} \rrbracket,\ \boldsymbol{\kappa})\mathrm{d}A \tag{5}$$

with Γ_i being the interface. In above equation the fracture energy for the interface in Equation (1) is used. ψ^e represents the elastic energy density. $\boldsymbol{\varepsilon}$ is the infinitesimal strain tensor, with components:

$$\varepsilon_{ij} = u_{(i,j)} = \frac{1}{2}\left(\frac{\partial u_i}{\partial x_j} + \frac{\partial u_j}{\partial x_i}\right) \tag{6}$$

Substituting Equation (4) into (5) yields the regularised energy functional for the solid:

$$\Psi_{\text{pot}} = \int_{\Omega} \psi^e\left(\boldsymbol{\varepsilon}^e(\mathbf{u}),\ \beta\right)\mathrm{d}V + \int_{\Omega} \mathcal{G}(\boldsymbol{\upsilon},\ \boldsymbol{\kappa})\delta_c(x_n)\mathrm{d}V \tag{7}$$

with the displacement jump $\llbracket \mathbf{u} \rrbracket$ being replaced by $\boldsymbol{\upsilon}$. In addition, the infinitesimal strain $\boldsymbol{\varepsilon}$ has been substituted by the 'elastic' strain $\boldsymbol{\varepsilon}^e$. This is due to the smeared representation of the discrete interface Γ_i, where the clear boundary between the bulk and the interface vanishes. There is no difference between the bulk and interface kinematics, that is, the infinitesimal strain, Equation (6), in the velocity of the interface Γ_i.

The displacement $\mathbf{u}(\mathbf{x})$ is then obtained from the variational principle for minimising Ψ_{pot}:

$$\mathbf{u}(\mathbf{x}) = \text{Arg}\left\{\inf_{\mathbf{u}\in\mathcal{S}_u}\left(\Psi_{\text{pot}} - W^{\text{ext}}\right)\right\} = \text{Arg}\left\{\inf_{\mathbf{u}\in\mathcal{S}_u}\left(\Psi_{\text{pot}} - \int_{\Gamma_t} \hat{\mathbf{t}}\cdot\mathbf{u}\mathrm{d}\Gamma\right)\right\} \tag{8}$$

in which $\mathcal{S}_u = \left\{\mathbf{u} \;\middle|\; \mathbf{u}(\mathbf{x}) = \bar{\mathbf{u}} \quad \forall \mathbf{x} \in \Gamma_u\right\}$. $\hat{\mathbf{t}}$ and $\bar{\mathbf{u}}$ are prescribed tractions and displacements.

2.2 | Elastic strain in a smeared sense

The weak form for $\mathbf{u} \in \mathcal{S}_u$ can be derived as:

$$\int_{\Omega} \frac{\partial \psi^e}{\partial \boldsymbol{\varepsilon}^e} : \boldsymbol{\varepsilon}^e(\delta\mathbf{u})\mathrm{d}V + \int_{\Omega} \frac{\partial \mathcal{G}(\boldsymbol{\upsilon},\ \boldsymbol{\kappa})}{\partial \boldsymbol{\upsilon}} \cdot \delta\boldsymbol{\upsilon}\delta_c(x_n)\mathrm{d}V = \delta W^{\text{ext}} \tag{9}$$

and we define the Cauchy stress and cohesive traction as

$$\sigma_{ij} = \frac{\partial \psi^e}{\partial \varepsilon^e_{ij}} \qquad \text{and} \qquad t_i = \frac{\partial \mathcal{G}}{\partial \upsilon_i}. \tag{10}$$

In cohesive-zone models, tractions $\mathbf{t} = [t_1,\ t_2]$ are explicitly linked to the displacement jump $\boldsymbol{\upsilon}$. In this study, the Xu–Needleman law is used,[41] defining the traction in the normal and shear direction as:

$$\begin{aligned} t_n &= \frac{\mathcal{G}_c}{\delta_n}\frac{\llbracket \upsilon_n \rrbracket}{\delta_n}\exp\left(-\frac{\llbracket \upsilon_n \rrbracket}{\delta_n}\right)\exp\left(-\frac{\llbracket \upsilon_s \rrbracket^2}{\delta_s^2}\right) \\ t_s &= \frac{2\mathcal{G}_c}{\delta_s}\frac{\llbracket \upsilon_s \rrbracket}{\delta_s}\left(1 + \frac{\llbracket \upsilon_n \rrbracket}{\delta_n}\right)\exp\left(-\frac{\llbracket \upsilon_n \rrbracket}{\delta_n}\right)\exp\left(-\frac{\llbracket \upsilon_s \rrbracket^2}{\delta_s^2}\right), \end{aligned} \tag{11}$$

which relates to the tractions $\mathbf{t}$ in Equation (10) and the displacement jump $\boldsymbol{\upsilon}$ via a standard transformation:

$$\mathbf{t} = \mathbf{R}^{\mathrm{T}}\mathbf{t}_d = \mathbf{R}^{\mathrm{T}}[t_s,\ \ t_n]^{\mathrm{T}}, \qquad \llbracket \boldsymbol{\upsilon} \rrbracket = [\llbracket \upsilon_s \rrbracket,\ \ \llbracket \upsilon_n \rrbracket]^{\mathrm{T}} = \mathbf{R}\boldsymbol{\upsilon} = \mathbf{R}[\upsilon_1,\ \ \upsilon_2]^{\mathrm{T}} \tag{12}$$

in which δ_n and δ_s are parameters defined by $\delta_n = \mathcal{G}_c/(t_u e)$ and $\delta_s = \mathcal{G}_c/\left(t_u\sqrt{\frac{1}{2}}e\right)$ with $e = \exp(1)$. t_u and $\mathcal{G}_c$ represent the fracture strength and fracture toughness, respectively. $[\![v_n]\!]$ and $[\![v_s]\!]$ are the displacement jump in the normal and shear direction, separately; $\mathbf{R}$ denotes the rotation matrix.[42] To prevent interpenetration, a penalty stiffness k_p is specified in the normal direction of the interface Γ_i. Other forms of the cohesive law can be considered in the analysis, including mode-mixity, but in the current study the focus is on the phase-field modelling of the cohesive interface.

Applying the divergence theorem to Equation (9) yields the elastic strain $\boldsymbol{\varepsilon}^e$[19,25]:

$$\varepsilon^e_{ij} = u_{(i,j)} - \mathrm{sym}\left(v_i n_j\right)\delta_c \tag{13}$$

with n_j being the component of the unit vector normal to the interface Γ_i. Obviously, the 'elastic' strain $\boldsymbol{\varepsilon}^e$ is composed of the displacement gradient and the term related to the displacement jump. Chen and de Borst[24] have proven that Equation (13) has an identical form as the regularised extended finite element method (XFEM).

2.3 | Governing equations for the displacement

Substituting Equation (13) into (9) leads to

$$\int_\Omega \left(\sigma_{ij}\delta \mathrm{u}_{(i,j)} - \delta_c\sigma_{ij}\mathrm{sym}\left(\delta v_i n_j\right) + t_i(\boldsymbol{v},\ \boldsymbol{\kappa})\delta_c\delta v_i +\right)\mathrm{d}V = \int_{\Gamma_t}\hat{t}_i\delta u_i \mathrm{d}A. \tag{14}$$

Applying the integration by parts, we reformulate Equation (14) as:

$$\int_\Omega \left(-\frac{\sigma_{ij}}{\partial x_j}\delta u_i - \left[\delta_c\left(\sigma_{ij}n_j - t_i(\boldsymbol{v},\ \boldsymbol{\kappa})\right)\right]\delta v_i\right)\mathrm{d}V = \int_{\Gamma_t}\left(\hat{t}_i - \sigma_{ij}n_j\right)\delta u_i \mathrm{d}A. \tag{15}$$

Considering a variation in the displacement field yields the strong form of the cohesive interface problem in the framework of the phase field method:

$$\begin{cases} \dfrac{\partial\sigma_{ij}}{\partial x_j} = 0 & \mathbf{x}\in\Omega, \quad (16a)\\ \sigma_{ij}n_j = \hat{t}_i & \mathbf{x}\in\Gamma_t, \quad (16b)\\ \delta_c\left(t_i(\boldsymbol{v},\ \boldsymbol{\kappa}) - \sigma_{ij}n_j\right) = 0 & \mathbf{x}\in\Omega. \quad (16c)\end{cases}$$

Equation (16a) is standard, and is supplemented by the constitutive relation, Equation (10). Equation (16c) is an additional equation for the smeared interface problem and represents the force equilibrium over the smeared interface. We have the traction balance relation $t_i(\boldsymbol{v},\ \boldsymbol{\kappa}) = \sigma_{ij}n_j$ in the smeared interface Γ_i^ξ. In the limiting case, when $\ell \to 0$, the discrete cohesive traction balance equation is recovered: $t_i([\![\mathbf{u}]\!],\ \boldsymbol{\kappa}) = \sigma_{ij}n_j$. Outside the smeared interface Γ_i^ξ, the Dirac-delta function is $\delta_c = 0$. The traction balance relation $t_i(\boldsymbol{v},\ \boldsymbol{\kappa}) = \sigma_{ij}n_j$ may not be satisfied, but the Dirac-delta function δ_c equals zero, guaranteeing the balance equation (16c).

3 | SMEARED REPRESENTATION OF THE DISCONTINUITY

The (discrete) interface Γ_i is now approximated by a smeared one Γ_i^ξ, see Figure 1. The smeared interface Γ_i^ξ is associated with a fixed phase field $d(\mathbf{x})$ around the interface Γ_i^ξ. $d(\mathbf{x})$ equals 1 at the centre of Γ_i^ξ, and vanishes from Γ_i. The width of the smeared interface is governed by a regularisation parameter ℓ. The phase field $d(\mathbf{x})$ is obtained by solving the variational problem:

$$d(\mathbf{x}) = Arg\left\{\inf_{d\in S_d}\quad \Gamma_\ell(d)\right\} \tag{17}$$

in which $S_d = \left\{ d \;\middle|\; d(\mathbf{x}) = 1 \;\; \forall \mathbf{x} \in \Gamma_c \right\}$ and

$$\Gamma_\ell(d) = \int_\Omega \gamma_d(d) \mathrm{d}V, \tag{18}$$

where $\Gamma_\ell(d)$ denotes the crack length, that is, the length of crack interface per unit area. $\gamma_d(d)$ represents the crack density function per unit volume. Herein, the following crack density function is employed[18]:

$$\gamma_d(d) = \frac{1}{\pi\ell}\left(2d(\mathbf{x}) - d(\mathbf{x})^2\right) + \frac{\ell}{\pi}\nabla d(\mathbf{x}) \cdot \nabla d(\mathbf{x}), \tag{19}$$

The Euler–Lagrange equation associated with the variational equation (17) is given as

$$\begin{aligned} 1 - d(x_n) - \ell^2 \frac{\mathrm{d}^2 d(x_n)}{\mathrm{d}x_n^2} = 0 \qquad & x_n \in \mathbb{R} \\ d = 1 \qquad & x_n = 0 \\ d = 0 \qquad & x_n = (-\infty,\; -\pi\ell/2] \bigcup [\pi\ell/2, +\infty) \end{aligned} \tag{20}$$

with the solution:

$$d(x_n) = \begin{cases} 1 - \sin\left(\dfrac{|x_n|}{\ell}\right) & -\pi\ell/2 \le x_n \le \pi\ell/2 \\ 0 & \text{otherwise} \end{cases} \tag{21}$$

with $x_n = (\mathbf{x} - \mathbf{x}_i) \cdot \boldsymbol{n}(\mathbf{x}_i)$, point $\mathbf{x}_i$ on the interface Γ_i and $\boldsymbol{n}(\mathbf{x}_i)$ the unit vector normal to Γ_i.

For the cohesive fracture model, the Dirac-delta function, $\delta_c(x_n)$ in Equation (3), can be approximated by the crack-density function in Equation (18).[24] To further simplify $\delta_c(x_n)$ we propose following form as an approximation:

$$\begin{aligned} \delta_c(x_n) = \frac{1}{2}\left|\frac{\mathrm{d}d(x_n)}{\mathrm{d}x_n}\right| &= \frac{1}{2}\begin{cases} -\dfrac{\mathrm{d}d(x_n)}{\mathrm{d}x_n} & 0 < x_n \le \pi\ell/2 \\ \dfrac{\mathrm{d}d(x_n)}{\mathrm{d}x_n} & -\pi\ell/2 \le x_n \le 0 \\ 0 & \text{otherwise} \end{cases} \\ &= \frac{1}{2}\begin{cases} \dfrac{1}{\ell}\cos\left(\dfrac{x_n}{\ell}\right) & -\pi\ell/2 \le x_n \le \pi\ell/2 \\ 0 & \text{otherwise} \end{cases} \end{aligned} \tag{22}$$

in which the fraction $\frac{1}{2}$ stems from the identity constraint of the Dirac-delta function, that is, $\int_{-\infty}^{\infty} \delta_c(x_n)\mathrm{d}x_n = 1$.

In Reference 19 the phase field $d(x_n)$ was prescribed numerically in the domain by solving the Euler–Lagrange equation (20). However, solving the Euler–Lagrange equation numerically is not favourable for the analysis due to the imposition of Dirichlet boundary conditions on the phase-field variable.[24] In addition, even with an exact imposition of the boundary conditions, the numerical results will still be slightly different from the analytical solutions.[24] Since analytical solutions of the Euler–Lagrange equation are available, that is, Equation (21), we can directly use them in the analysis. In a pre-processing step, we only need to store the distance between the interface and Gauss points once. Then, in the nonlinear solution scheme, we utilise the stored distance and Equation (22) to compute the Dirac-delta function.

In Figure 2 we have plotted the phase field $d(x_n)$, the crack density function $\gamma_d(d)$ and the Dirac-delta function $\delta_c(x_n)$. The distribution of $d(x_n)$, $\gamma_d(d)$ and $\delta_c(x_n)$ narrows around the interface Γ_i, confining the influence of the smeared interface Γ_i^ξ locally. In References 19 and 25, the support of $d(x_n)$ is spread over the entire domain, that is, it covers the range $[-\infty,\; \infty]$. This is due to the use of a particular variant of the phase-field model, now known as AT2, in simulations of

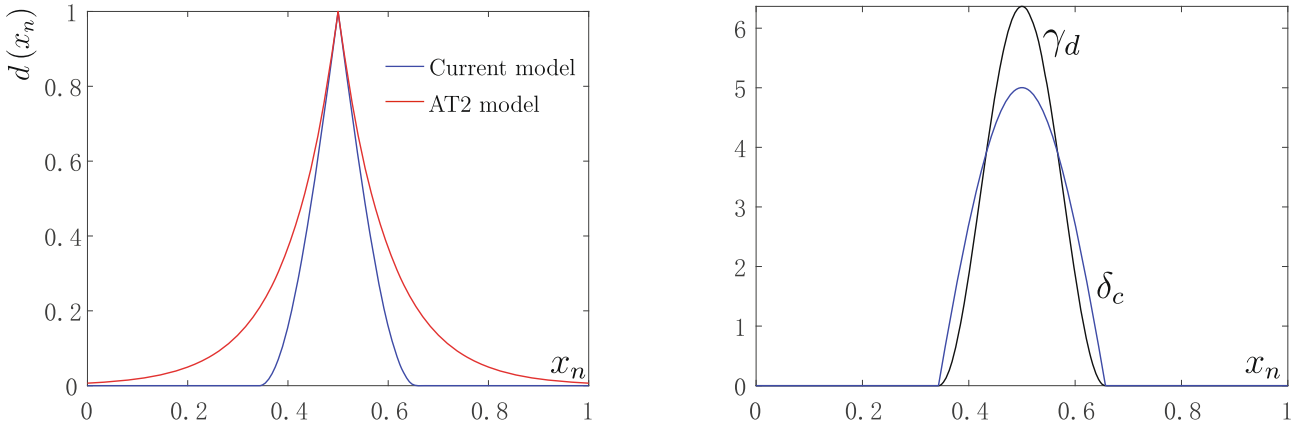

FIGURE 2 One-dimensional analytical phase field $d(\mathbf{x})$, crack density function γ_d, and Dirac-delta function δ_c for a uniaxial bar (length 1) with an interface Γ_i in the middle. The regularization length is $\ell = 0.1$.

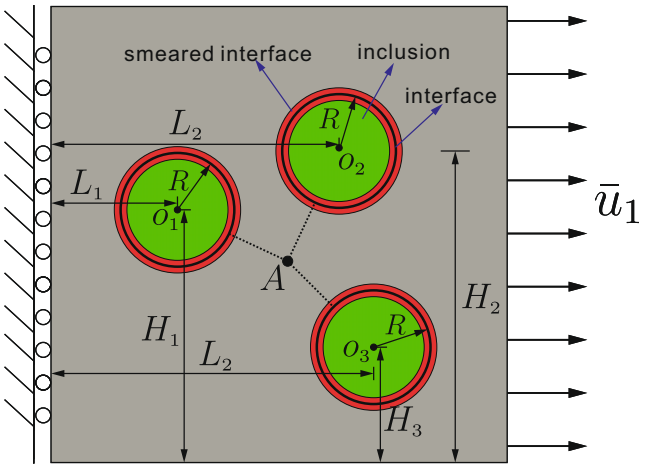

FIGURE 3 Traction test of a micro-structure containing inclusions. Red areas denote the smeared interface. Black circles represent the interface between inclusions and matrix.

Verhoosel and de Borst[19] and of Nguyen et al.[25] This is a superior aspect of the current model compared to the AT2 phase-field model.

Another deficiency of the use of the AT2 model is that a situation can arise in which a point in the domain, for example, point A in Figure 3, has the same distance to several interfaces. In Figure 3 this happens to point A. In such a situation it is unclear which interface should be used when evaluating the fracture energy and the stiffness matrix at point A. There is no issue in the current model, due to the local support of the phase field, as illustrated in Figure 2. Only points inside the smeared interface, that is, the red areas in Figure 3, will be considered when computing the fracture energy and the stiffness matrix.

4 | SMEARED DISPLACEMENT JUMP ACROSS THE INTERFACE

In this section we will construct the displacement jump in a smeared setting. The displacement jump relies on a distance parameter h. The optimal value of h will be derived. The displacement jump error will be presented to study the influence of h.

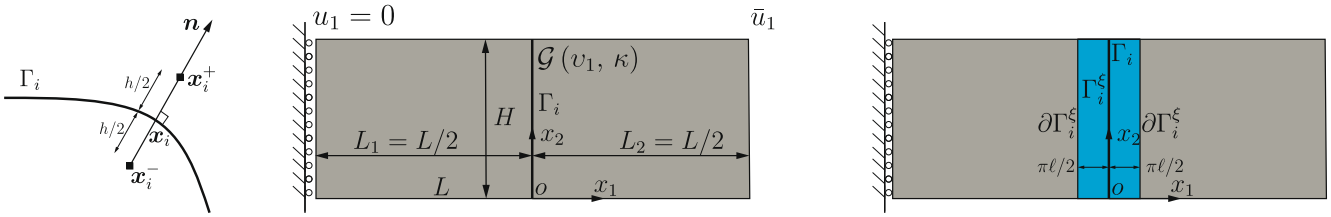

FIGURE 4 (A) approximation of the displacement jump across the interface Γ_i; (B) uniaxial traction of a bar with an interface Γ_i; (C) smeared interface Γ_i^ξ (blue area). Due to the setup of the problem in (B), only mode-I crack opening υ_1 is included in the analysis. The fracture energy function is given as: $\mathcal{G}(\upsilon_1, \kappa)$.

4.1 | Displacement jump in a smeared setting

In the phase-field model the interface Γ_i only exists in a smeared sense. The displacement jump $[\![\mathbf{u}]\!](\mathbf{x}_i)$ in the fracture energy function $\mathcal{G}([\![\mathbf{u}]\!], \boldsymbol{\kappa})$ is defined for the discrete interface, see Equation (2). Thus, we need to approximate the displacement jump $[\![\mathbf{u}]\!](\mathbf{x}_i)$ in a smeared sense. In the regularisation framework, the displacement filed $\mathbf{u}$ is continuous in the whole domain. We can therefore approximate the displacement field around the interface Γ_i, see Figure 4A, by employing a first-order Taylor expansion of $\mathbf{u}$ at the interface:

$$\begin{aligned}\mathbf{u}\left(\mathbf{x}_i + \frac{h}{2}\boldsymbol{n}^i\right) &\approx \mathbf{u}(\mathbf{x}_i) + \frac{h}{2}\nabla\mathbf{u}\boldsymbol{n}^i,\\ \mathbf{u}\left(\mathbf{x}_i - \frac{h}{2}\boldsymbol{n}^i\right) &\approx \mathbf{u}(\mathbf{x}_i) - \frac{h}{2}\nabla\mathbf{u}\boldsymbol{n}^i\end{aligned} \tag{23}$$

with $\mathbf{x}_i$ being a point on the interface Γ_i, $\boldsymbol{n}^i$ being the unit normal vector to the interface Γ_i, and h being a distance parameter. Subsequently, we can approximate the displacement jump of point $\mathbf{x}_i$ at the interface Γ_i as:

$$[\![\mathbf{u}]\!](\mathbf{x}_i) \approx \boldsymbol{\upsilon}(\mathbf{x}_i) = \mathbf{u}\left(\mathbf{x}_i + \frac{h}{2}\boldsymbol{n}^i\right) - \mathbf{u}\left(\mathbf{x}_i - \frac{h}{2}\boldsymbol{n}^i\right) = h\nabla\mathbf{u}\boldsymbol{n}^i \tag{24}$$

with $\boldsymbol{\upsilon}(\mathbf{x}_i) = [\upsilon_1, \upsilon_2]$ being the approximation of the displacement jump. Obviously, the parameter h should have a small value to guarantee the feasibility of the approximation in Equation (24). In next sub-section, we will derive the optimal value of h.

In the regularised context the displacement jump should be prescribed over the whole domain,[24,25] see the domain integration in Equation (4). However, our phase-field model, cf. Equation (21), narrows the influence of the interface and constrains it to a localised band, see Figure 3. Following the concept of the smeared surface area, Equation (3), we now regularise the displacement jump with the aid of the Dirac-delta function[24,25]:

$$[\![\mathbf{u}]\!](\mathbf{x}) \approx \int_{x_n=-\infty}^{\infty} \boldsymbol{\upsilon}(\mathbf{x})\delta_c(x_n)\mathrm{d}x_n = \int_{x_n=-\pi\ell/2}^{\pi\ell/2} \boldsymbol{\upsilon}(\mathbf{x})\delta_c(x_n)\mathrm{d}x_n \tag{25}$$

with $x_n = (\mathbf{x} - \mathbf{x}_i)\cdot\boldsymbol{n}(\mathbf{x}_i)$; $\boldsymbol{\upsilon}(\mathbf{x})$ denotes the displacement jump approximation at point $\mathbf{x}$. The establishment of the regularized form in Equation (25) requires that $\boldsymbol{\upsilon}(\mathbf{x})$ should be constant in the direction normal to the interface:

$$\frac{\partial\boldsymbol{\upsilon}}{\partial x_n} = 0 \tag{26}$$

yielding

$$\boldsymbol{\upsilon}(\mathbf{x}) = \boldsymbol{\upsilon}(\mathbf{x}_i + x_n\boldsymbol{n}) = \boldsymbol{\upsilon}(\mathbf{x}_i) \tag{27}$$

which indicates that we can directly use the displacement jump function in Equation (24) to compute the fracture energy in Equation (4). This avoids the introduction of an auxiliary field to represent the displacement jump in the cohesive interface model, being different from Verhoosel and de Borst's method.[19] In their approach, the displacement jump is considered as an independent variable (auxiliary field) in the computation, and must be presented in the entire domain.[24]

4.2 | Optimal distance parameter h

To derive the optimal distance parameter h, we will consider a two-dimensional version of a uniaxial tension problem, as illustrated in Figure 4B. The plate is characterised by a Young's modulus E. An interface Γ_i is prescribed in the centre of the plate. Due to the set-up of the problem, only mode-I crack opening υ_1 has to be included in the analysis. The fracture energy is given as $\mathcal{G}(\upsilon_1,\ \kappa) = \frac{1}{2}k\upsilon_1^2$, yielding the traction $t_1 = k\upsilon_1$, with k being the interface stiffness. The analytical solutions for the displacement, the displacement jump and the stress can be derived as:

$$u_1(x_1,\ x_2) = \begin{cases} \dfrac{k\upsilon_1}{E}x_1 + \dfrac{k\upsilon_1}{E}\dfrac{L}{2} & -L/2 \le x_1 \le 0^-, \\ \dfrac{k\upsilon_1}{E}x_1 + \left(\bar{u}_1 - \dfrac{k\upsilon_1}{E}\dfrac{L}{2}\right) & 0^+ \le x_1 \le L/2, \end{cases}$$
$$[[u]] = \upsilon_1 = \frac{\bar{u}_1 E}{kL + E}, \qquad \sigma_1(x_1,\ x_2) = \frac{\bar{u}_1 kE}{kL + E}, \tag{28}$$

where 0^- and 0^+ are the left and right side of the interface Γ_i. We refer to this solution as the discrete analytical solution.

For the phase-field regularised cohesive interface model, we can use the expression for the strain in Equation (13). For the problem stated in Figure 4B,C we then obtain the stress using Hooke's law (governing equation):

$$\sigma_1(x_1,\ x_2) = E\left(\frac{\mathrm{d}}{\mathrm{d}x_1}u_1(x_1,\ x_2) - \delta_c\upsilon_1\right) \tag{29}$$

with υ_1 being the displacement jump given in Equation (24); δ_c being Dirac-delta function defined in Equation (22). Then, the momentum balance equation (governing equation) reads:

$$\sigma_1(x_1,\ x_2) = E\left(\frac{\mathrm{d}}{\mathrm{d}x_1}u_1(x_1,\ x_2) - \delta_c\upsilon_1\right) = k\upsilon_1 \tag{30}$$

with $k\upsilon_1$ being the cohesive traction acting on the interface Γ_i.

In the regularised framework, the displacement is continuous in the whole domain. In solving Equation (30) we must use the boundary condition for the problem stated in Figure 4B: $u_1 = \bar{u}_1$ at $x_1 = L/2$ and $u_1 = 0$ at $x_1 = -L/2$. Furthermore, we should consider the continuous displacement field at the smeared interface boundary $\partial\Gamma_i^{\xi}$, that is, $x_1 = \pm\pi\ell/2$. Then, the displacement is given as:

$$u_1(x_1,\ x_2) = \begin{cases} \dfrac{k\upsilon_1}{E}x_1 + \left(\bar{u}_1 - \dfrac{k\upsilon_1}{E}\dfrac{L}{2}\right) & \pi\ell/2 \le x_1 \le L/2, \\ \dfrac{\upsilon_1}{2}\sin\left(\dfrac{x_1}{\ell}\right) + \dfrac{k\upsilon_1}{E}x_1 + \left(\dfrac{\upsilon_1}{2} + \dfrac{k\upsilon_1}{E}\dfrac{L}{2}\right) & -\pi\ell/2 < x_1 \le \pi\ell/2, \\ \dfrac{k\upsilon_1}{E}x_1 + \dfrac{k\upsilon_1}{E}\dfrac{L}{2} & -L/2 \le x_1 \le -\pi\ell/2. \end{cases} \tag{31}$$

We refer to this solution as the smeared analytical solution.

The displacement continuity condition at $x_1 = -\pi\ell/2$ is considered in deriving the above equation. If we take the displacement continuity condition at $x_1 = \pi\ell/2$ into account we can compute the displacement

jump υ_1:

$$\upsilon_1 = \frac{\bar{u}_1 E}{kL + E} \tag{32}$$

which is equal to the analytical solution of υ_1 in Equation (28).

To obtain the optimal distance parameter h, we use Equation (24) to compute the displacement jump υ_1:

$$\upsilon_1 = h\nabla \mathbf{u}\boldsymbol{n}^i = h\left(\frac{\upsilon_1}{2}\frac{1}{\ell}\cos\left(\frac{x_1}{\ell}\right)\Big|_{x_1=0} + \frac{k\upsilon_1}{E}\right) = h\left(\frac{\upsilon_1}{2}\frac{1}{\ell} + \frac{k\upsilon_1}{E}\right) \tag{33}$$

which yields

$$h = \frac{2\ell}{1 + 2k\ell/E}. \tag{34}$$

In engineering practice, it normally holds that $2k\ell/E \ll 1$, due to the small values of interface stiffness k[33] and the regularisation length ℓ[25] compared to the large value of Young's modulus E, for example, for epoxy of composites $E \approx 4$GPa and $E \approx 20$GPa for concrete.[9] This approximation yields an approximated optimal distance parameter:

$$h = 2\ell \tag{35}$$

which is independent of the shape of the cohesive-zone law.

Next, we study the influence of the distance parameter h and validate the optimal form of h as given by Equation (35). We consider the uniaxial tension problem in Figure 4B. With a suitable re-scaling of the loading $E_0 = 99.0$. A unit cross-sectional area $A = 1$ is considered with a height $H = 1$ and a length $L = 1$. The interface stiffness is $k = 1$ and the prescribed displacement is $\bar{u}_1 = 1$ at $x_1 = L/2$. The plate has been discretised by the triangulation in Figure 5. We will employ finite elements to solve the problem, see Section 5. In particular, we use C^1-continuous Powell-Sabin B-splines, which are based on triangles, for the spatial discretisation.[42,47] The C^1-continuity assures an improved stress prediction.[48] To well represent the interface in a smeared sense, the regularisation length is chosen as $l \geq 4h$ (h: element size around the crack).[20] The distribution of the phase field $d(\mathbf{x})$ along the interface is shown in Figure 5, prescribed analytically by Equation (21).

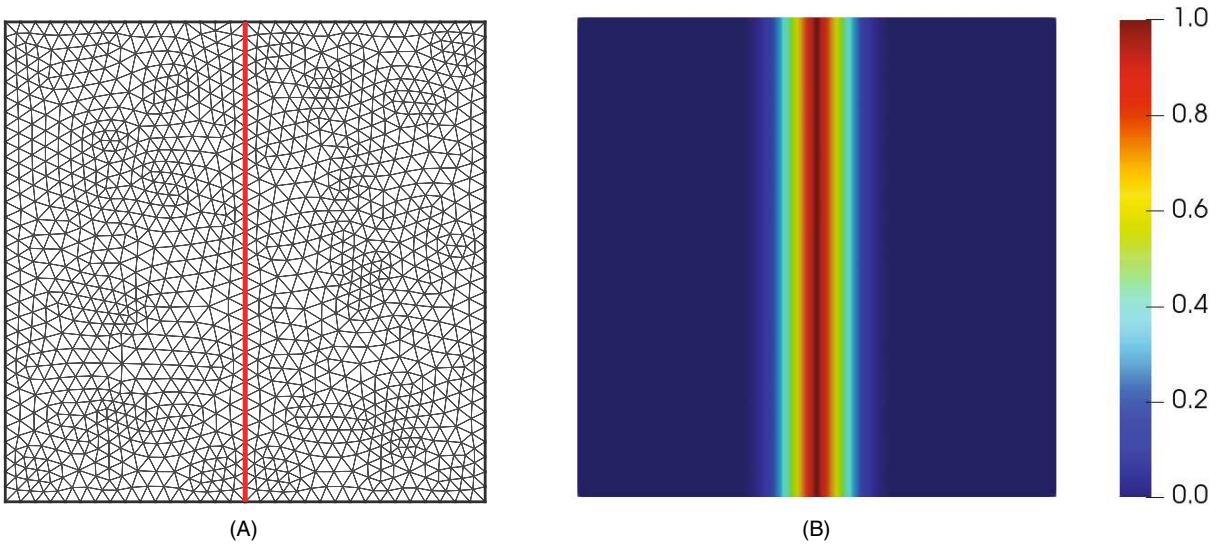

FIGURE 5 Initial triangulation of the plate and contour plot of the phase field prescribed along the interface. The regularisation length is chosen as $l = 0.1$. (A) Initial triangulation (B) contour plot of phase field $d(\mathbf{x})$.

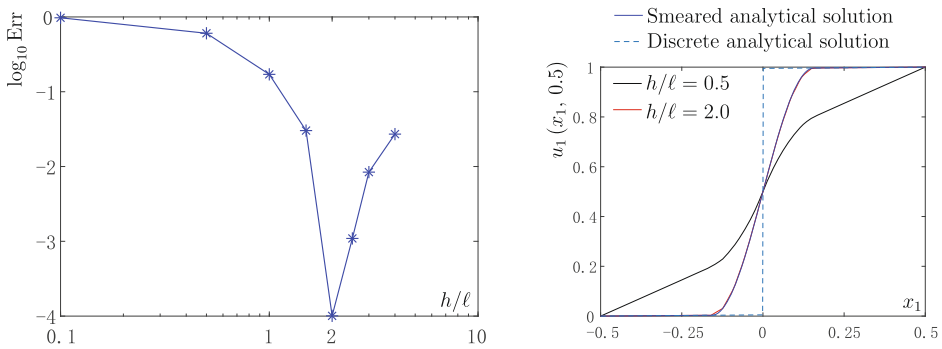

FIGURE 6 Displacement jump error Err and displacement u_1.

Figure 6 shows the comparison between the numerical and the analytical solutions. To study the influence of the distance parameter h, we define the relative displacement jump with respect to the analytical solution as:

$$\text{Err} = \sqrt{\frac{\int_{\Gamma_i^\xi} \left(v_1^h - v_1^a\right)^2 \mathrm{d}V}{\int_{\Gamma_i^\xi} \left(v_1^a\right)^2 \mathrm{d}V}} \tag{36}$$

with Γ_i^ξ being the smeared interface, also see Figure 4C, v_1^h being the numerical solution, v_1^a being the discrete analytical solution in Equation (28).

Figure 6A shows that for increasing values of h, the relative error Err first reduces to a small value and then increases. A similar behaviour is observed in Nguyen's analysis.[25] The smallest relative error Err is obtained in setting the distance parameter $h = 2\ell$, yielding support to the validity of Equation (34). Figure 6B presents the distribution of the displacement u_1. For $h = 2\ell$ the numerical solution tends towards the smeared analytical solution, derived in Equation (31), whereas for $h = 0.5\ell$ the numerical solution diverges from the smeared analytical solution.

5 | FINITE ELEMENT IMPLEMENTATION

To solve Equation (16), the finite element method is used. In the simulation, we need to solve the displacement field $\mathbf{u}$. The displacement jump $\boldsymbol{v}$, linked to the interface Γ_i, can be inferred from Equation (24). The phase field d, used to regularise the interface Γ_i, is obtained from Equation (21) and prescribed analytically along Γ_i, see Section 3.

In the examples we have used C^1-continuous Powell-Sabin B-splines to discretise the domain.[42,47] Standard (C^0-continuous) finite elements could have been used equally well, but the C^1-continuity ensures an improved stress prediction, which is highly advantageous for predicting the correct direction of the crack path.[48] Powell-Sabin B-splines describe the geometry and interpolate the displacement field $\mathbf{u}$ in an isoparametric sense[42]:

$$\boldsymbol{x} = \sum_{k=1}^{N_v} \sum_{j=1}^{3} N_k^j \boldsymbol{x}_k^j = \boldsymbol{N}\boldsymbol{x} \qquad \mathbf{u} = \sum_{k=1}^{N_v} \sum_{j=1}^{3} N_k^j \boldsymbol{U}_k^j = \boldsymbol{N}\boldsymbol{U}, \tag{37}$$

where $\boldsymbol{x}_k^j$ represent the coordinates of the corners $\boldsymbol{Q}_k^j$ of the Powell-Sabin triangles, $\boldsymbol{U}_k^j$ denotes the degrees of freedom at $\boldsymbol{Q}_k^j$, and N_v is the total number of vertices. The indices $j = 1, 2, 3$ imply that three Powell-Sabin B-splines N_k^j are defined on each vertex k. $\boldsymbol{N}$, $\boldsymbol{x}$ and $\boldsymbol{U}$ are the shape function matrix of the displacement, the vector of the coordinates and the displacement, respectively.

In a two-dimensional setting we introduce the stress and the strain in a Voigt notation: $\boldsymbol{\sigma} = \{\sigma_{11};\ \sigma_{22};\ \tau_{12}\}^{\mathrm{T}}$ and $\boldsymbol{\varepsilon} = \{\varepsilon_{11};\ \varepsilon_{22};\ \gamma_{12}\}^{\mathrm{T}}$. With the Powell-Sabin interpolation of Equation (37), we have $\boldsymbol{\varepsilon}(\mathbf{x}) = \boldsymbol{B}_u(\mathbf{x})\boldsymbol{U}$. The displacement

jump $\boldsymbol{\upsilon}$ in Equation (24) is then discretised as

$$\boldsymbol{\upsilon}(\mathbf{x}) = h\mathbf{n}\tilde{\boldsymbol{B}}_u(\mathbf{x}_i)\boldsymbol{U} \tag{38}$$

with

$$\mathbf{n} = \begin{bmatrix} n_1 & n_2 & 0 & 0 \\ 0 & 0 & n_1 & n_2 \end{bmatrix} \tag{39}$$

and n_1 and n_2 being components of the normal vector $\boldsymbol{n}$ to the interface Γ_i. $\tilde{\boldsymbol{B}}_u(\mathbf{x}_i)$ is the matrix which contains the derivatives of the shape functions. $\mathbf{x}_i$ is the perpendicular foot from the point $\mathbf{x}$ to the interface Γ_i.

$$\left\{\frac{\partial u_1}{\partial x_1};\ \frac{\partial u_1}{\partial x_2};\ \frac{\partial u_2}{\partial x_1};\ \frac{\partial u_2}{\partial x_2}\right\}^{\mathrm{T}} = \tilde{\boldsymbol{B}}_u\boldsymbol{U}. \tag{40}$$

In Equation (13) there is a term related to the displacement jump: $\mathrm{sym}(\boldsymbol{\upsilon}\otimes\boldsymbol{n})\delta_c = \mathrm{sym}\left(\upsilon_i n_j\right)\delta_c$. Substituting Equation (38) into this expression yields

$$\mathrm{sym}(\boldsymbol{\upsilon}\otimes\boldsymbol{n})\delta_c = h\delta_c\mathbf{M}\tilde{\boldsymbol{B}}_u(\mathbf{x}_i)\boldsymbol{U} \tag{41}$$

with

$$\mathbf{M} = \begin{bmatrix} n_1^2 & n_1n_2 & 0 & 0 \\ 0 & 0 & n_1n_2 & n_2^2 \\ \dfrac{n_1n_2}{2} & \dfrac{n_2^2}{2} & \dfrac{n_1^2}{2} & \dfrac{n_1n_2}{2} \end{bmatrix}. \tag{42}$$

Now, we can obtain the system of non-linear equations from the variational expression, Equation (14):

$$\boldsymbol{F}_{\mathrm{int},u}(\boldsymbol{U}) = \boldsymbol{F}_{\mathrm{ext},u} = \int_{\Gamma_t}\boldsymbol{N}^{\mathrm{T}}\hat{\mathbf{t}}\mathrm{d}\Gamma \tag{43}$$

with the internal force vectors:

$$\begin{aligned}\boldsymbol{F}_{\mathrm{int},u}(\boldsymbol{U}) = &\int_\Omega\left[\boldsymbol{B}_u^{\mathrm{T}} - h\delta_c\tilde{\boldsymbol{B}}_u^{\mathrm{T}}(\mathbf{x}_i)\mathbf{M}^{\mathrm{T}}\right]\mathbf{D}\left[\boldsymbol{B}_u - h\delta_c\mathbf{M}\tilde{\boldsymbol{B}}_u(\mathbf{x}_i)\right]\mathrm{d}V\cdot\boldsymbol{U} \\ &+\int_\Omega h\delta_c\tilde{\boldsymbol{B}}_u^{\mathrm{T}}\boldsymbol{N}^{\mathrm{T}}\mathbf{t}\mathrm{d}V\end{aligned} \tag{44}$$

with $\mathbf{D}$ being the elasticity matrix, δ_c being the approximated Dirac-delta function defined in Equation (22), and $\mathbf{t}$ being the cohesive traction given in Equation (12). Then, Equation (43) is solved by a standard Newton–Raphson procedure with the tangent stiffness matrix:

$$\begin{aligned}\mathbf{K}_{uu} = &\int_\Omega\left[\boldsymbol{B}_u^{\mathrm{T}} - h\delta_c\tilde{\boldsymbol{B}}_u^{\mathrm{T}}(\mathbf{x}_i)\mathbf{M}^{\mathrm{T}}\right]\mathbf{D}\left[\boldsymbol{B}_u - h\delta_c\mathbf{M}\tilde{\boldsymbol{B}}_u(\mathbf{x}_i)\right]\mathrm{d}V \\ &+\int_\Omega h^2\delta_c\tilde{\boldsymbol{B}}_u^{\mathrm{T}}\boldsymbol{N}^{\mathrm{T}}\frac{\partial\mathbf{t}}{\partial\boldsymbol{\upsilon}}\boldsymbol{N}\tilde{\boldsymbol{B}}_u\mathrm{d}V.\end{aligned} \tag{45}$$

The overall algorithm reads as follows:

1. **Initialization**
   (1.1) Initialize the displacement $\boldsymbol{U}_0$.

(1.2) Find the perpendicular foot $\mathbf{x}_i$ from Gauss points $\mathbf{x}_g$ to the interface Γ_i, correspondingly get the normal vector $\boldsymbol{n}(\mathbf{x}_i)$ to Γ_i. Then obtain the matrix $\tilde{\boldsymbol{B}}_u(\mathbf{x}_i)$ in Equation (40).

(1.3) Find the distance $x_n = (\mathbf{x}_g - \mathbf{x}_i) \cdot \boldsymbol{n}(\mathbf{x}_i)$ between the interface Γ_i and Gauss points. The Dirac-delta function $\delta_c(x_n)$ is obtained from Equation (22).

2. **FOR** loading increment (pseudo time t^{n+1}).

Given $\boldsymbol{U}_n$. Apply the Newton–Raphson scheme to obtain the displacement $\boldsymbol{U}_{n+1}$. Equation (43) and (45) will be used.

6 | NUMERICAL EXAMPLES

Two examples are now presented to assess the performance of the approach. First, we will consider a 'H'-shaped plate under uniaxial traction with a cohesive interface in the centre. Then, a debonding test on a fibre-reinforced epoxy specimen is considered to explore interface debonding under mixed-mode loading conditions and to demonstrate the ability of the method to accurately handle curved interfaces. In order to properly represent the interface in a smeared sense the regularisation length has been chosen such that $l \geq 4h$ (h: element size around the crack).[20]

6.1 | 'H'-shaped plate under uniaxial traction

We consider an 'H'-shaped plate under uniaxial loading, Figure 7A. A cohesive interface is prescribed at the centre of the plate, and follows the Xu–Needleman relation, Equation (11). With a suitable re-scaling of the loading, we can set Young's modulus $E_0 = 1.0$, Poisson's ratio $\nu = 0.0$. A unit cross-sectional area $A = 1$ is considered with a height $H = 1$ and a length $L = 1$. In Figure 7A the discrete interface Γ_i is regularised as a smeared interface Γ_i^ξ (blue area) by the phase-field model of Section 3. The regularisation length is set as $\ell = 0.1$. A discrete interface model is used to provide the reference solution.[42]

Figures 7B and 8 show the comparison between the numerical solution and the reference solution. According to Figure 7B the displacements of the smeared model agree well with those of the discrete interface model, with exception of course of the displacement within the smeared interface Γ_i^ξ. The displacement plot shows a jump at the interface Γ_i in the discrete model, while it is smooth along DF in the smeared interface model. The force-displacement diagram in Figure 8 presents the relation between the horizontal resultant force F_{x_1} and the horizontal displacement $\bar{u}_1$ at the left edge. The 'smeared' solution compares well with the reference solution: the error level is below 1%.

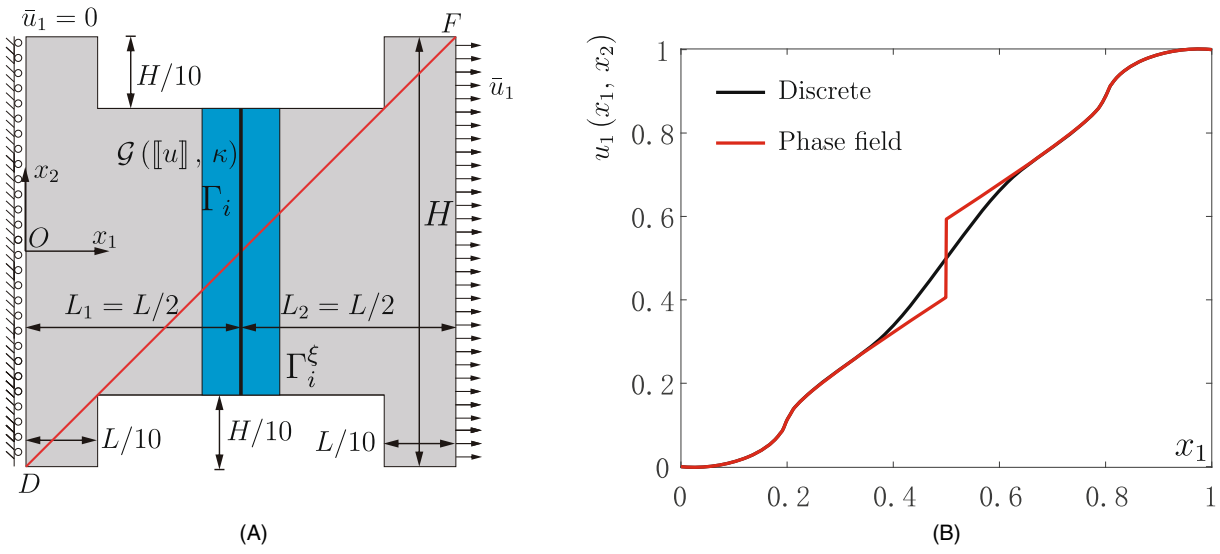

FIGURE 7 (A) Axial traction of a 'H'-shaped plate with an interface Γ_i; the blue area indicates the smeared interface Γ_i^ξ; (B) displacement u_1 along the diagonal line DF in (A).

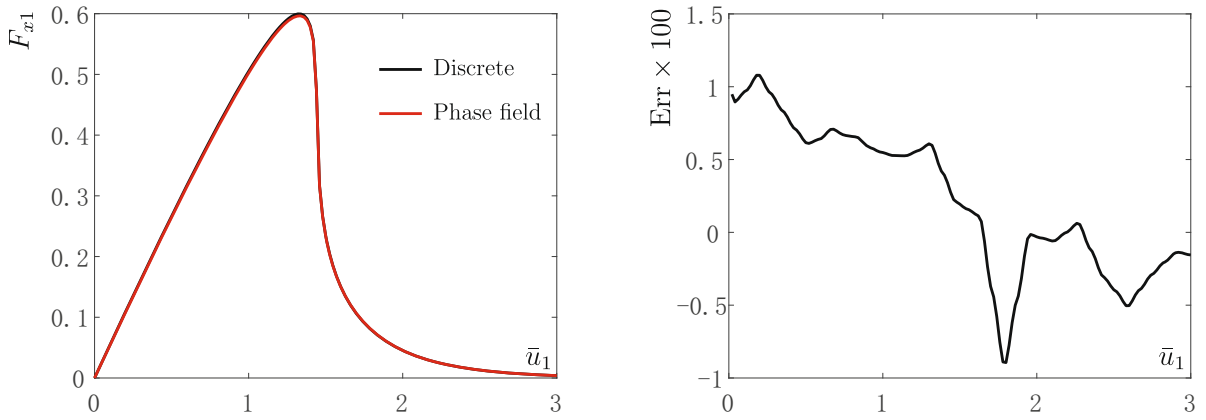

FIGURE 8 Force-displacement curve and Err $= \frac{F_{x_1}^{\text{num}} - F_{x_1}^{\text{ext}}}{F_{x_1}^{\text{ext}}}$, the error of the numerical solution, where 'num' denotes the results of the proposed method and 'ext' represents the discrete interface solution.

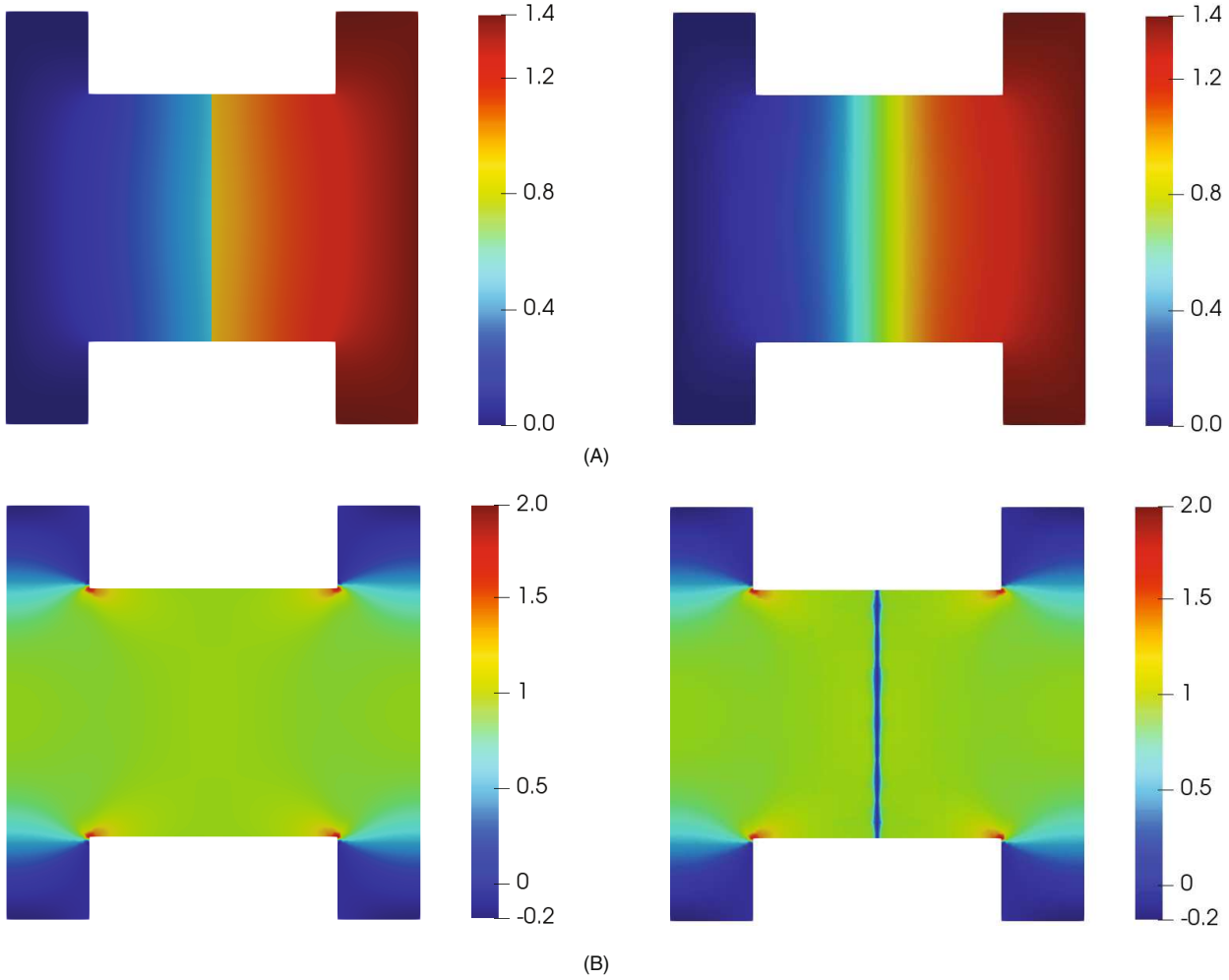

FIGURE 9 Contour plot of displacement u_1 and stress σ_1. The figures in the left column represent the solution of the discrete model, while the figures in the right column represent the solution of the 'smeared' model. (A) Contour plot of displacement u_1 (B contour plot of stress σ_1.

The contour plots of the displacement u_1 and stress σ_1 are given in Figure 9.The stresses and the displacements are almost identical in the whole domain, except for a discrepancy in the range of the smeared interface Γ_i^ξ, which is a direct consequence of the term $\boldsymbol{\sigma} = \left[\boldsymbol{B}_u - h\delta_c \mathbf{M}\tilde{\boldsymbol{B}}_u(\mathbf{x}_i)\right]\mathbf{D}\boldsymbol{U}$ in Equations (10) and (44). Indeed, the regularisation strategy causes zero stresses around the interface Γ_i due to the minus term in the equation for the stress.

6.2 | Fiber-epoxy debonding test

We now consider a problem of fibre-epoxy debonding to demonstrate the ability of the method to analyse mixed-mode cracks.[24] Plane-strain conditions have been assumed.[9] The geometry of the specimen is shown in Figure 10A. Due to symmetry, only one quarter of the specimen has been considered with symmetry-enforcing boundary conditions. The

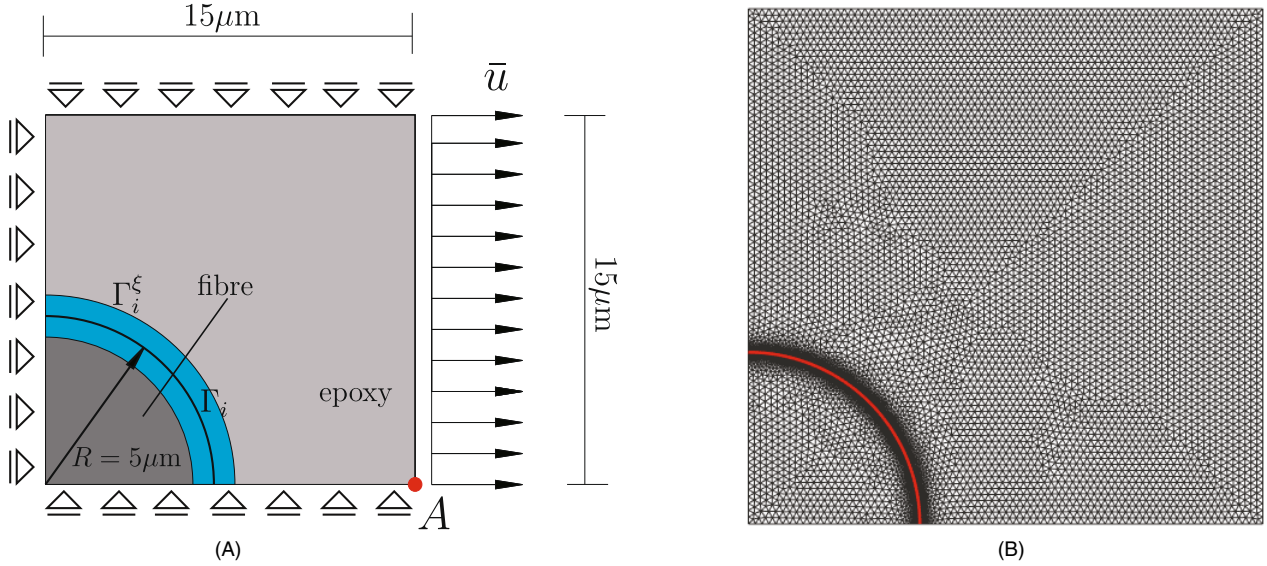

FIGURE 10 (A) Geometry and boundary conditions of one quarter of the fibre,[9] where the blue area indicates the smeared interface Γ_i^ξ; (b) initial triangulation with the smallest element size $e = 0.008\mu$m. To accurately describe Γ_i^ξ the mesh around the interface Γ_i is refined with the smallest element size e. In (B), the interface Γ_i is shown in red.

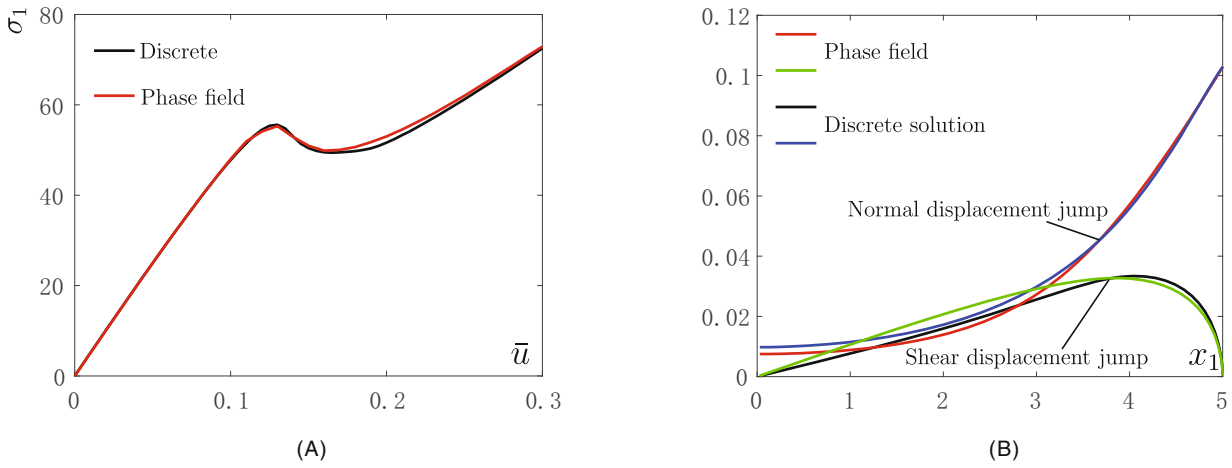

FIGURE 11 (A) Response curves for the plate. The stress component σ_1 at $\boldsymbol{x}_A = (15,\ \ 0)\mu$m is plotted *vs* the prescribed displacement $\bar{u}$. A discrete interface model is employed to provide the reference solution; (B) displacement jump (μm) along the interface Γ_i at the loading step $\bar{u} = 0.15\mu$m. The discrete interface model is employed to provide the reference solution.[9]

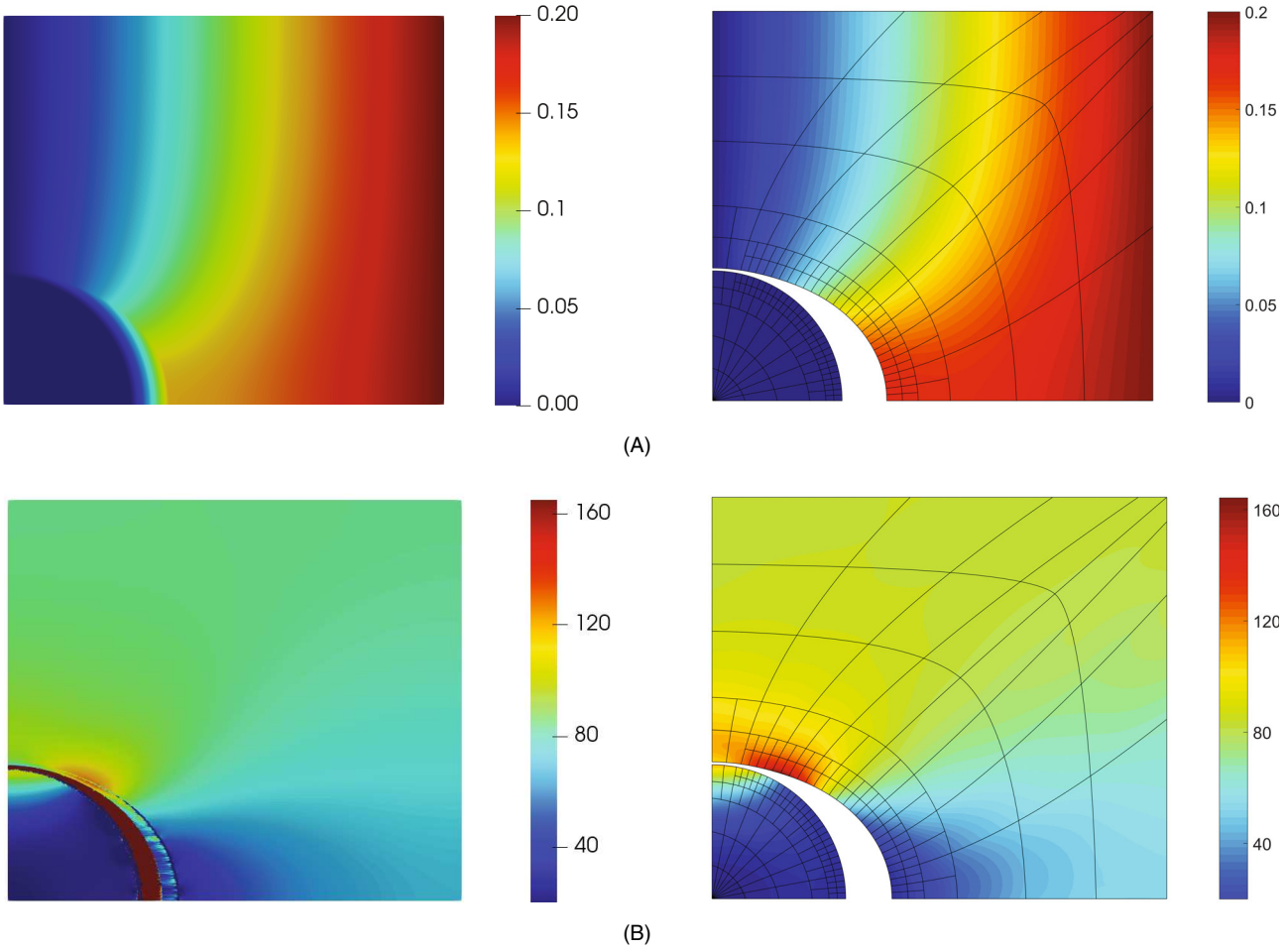

FIGURE 12 Distribution of the displacement u_1 and the stress σ_1 under the loading $\bar{u} = 0.2\mu$m. The displacements have been amplified by a factor 10. The left column denotes the solution of phase-field method, while the right column represents the solution of the discrete interface model. (A) u_1 contour plot (B) σ_1 contour plot.

material properties are as follows. For the fibre: Young's modulus $E = 225$ GPa and Poisson's ratio $\nu = 0.2$. For the epoxy: Young's modulus $E = 4.3$ GPa and a Poisson's ratio $\nu = 0.34$. The tractions at the fibre-epoxy interface have been assumed to follow the Xu–Needleman relation with $t_u = 50$ MPa and $\mathcal{G}_c = 4 \times 10^{-3}$ N/mm.

The response is presented in terms of the horizontal stress σ_1 at $\boldsymbol{x}_A = (15, \ \ 0)\mu$m as a function of the prescribed displacement $\bar{u}$, see Figure 11A. The results agree well with the solution of the discrete interface model.[9] Figure 11B shows the displacement jump obtained from the proposed method. The displacements and the stresses in the fibre and epoxy are shown in Figure 12. The results of the 'smeared' model compare well with those of the discrete interface model, though there are some oscillations in the plot around the smeared interface Γ_i^{ξ}.

In this example we could have considered failure in the matrix by introducing a surface energy function.[33,45,46] However, since our focus is on the interface failure modelling by the regularised phase-field model we have refrained from this.

7 | CONCLUDING REMARKS

In discrete cohesive interface models, the interfaces are treated as geometric discontinuities. To insert a new crack or interface, remeshing around crack tips is then required. Alternatively, the extended finite element method introduces enrichment functions to describe geometric discontinuities such as cracks. To avoid topological changes or the introduction of enrichment functions we propose a phase-field regularised cohesive interface model to arrive at a smeared

representation of the interface. Subsequently, the displacement jump is obtained by a first-order Taylor expansion of the displacement at the interface. Then, the cohesive zone law can be used directly in the analysis, similar to a fully discrete model.

The displacement jump function depends on the choice of a distance parameter. An optimal value of this parameter is derived from the analytical solution of a uniaxial tension problem. We have assessed the accuracy of the proposed method by comparing with the discrete interface solutions, featuring straight and curved interfaces.

CONFLICT OF INTEREST STATEMENT

The authors declare that there is no conflict of interest regarding the publication of this article.

DATA AVAILABILITY STATEMENT

Data sharing is not applicable to this article as no datasets were generated or analysed during this study.

ORCID

R. de Borst https://orcid.org/0000-0002-3457-3574

REFERENCES

1. Ren H, Qian Z, Lin B, Huang Q, Crispino M, Ketabdari M. Effect of recycled concrete aggregate features on adhesion properties of asphalt mortar-aggregate interface. *Constr Build Mater*. 2022;353(129):97.
2. Ngo D, Scordelis AC. Finite element analysis of reinforced concrete beams. *J Am Concrete Ins*. 1967;64:152-163.
3. Rashid YR. Analysis of reinforced concrete pressure vessels. *Nucl Eng Des*. 1968;7:334-344.
4. de Borst R. Some recent issues in computational failure mechanics. *Int J Numer Methods Eng*. 2001;52:63-95.
5. Schellekens JCJ, de Borst R. On the numerical integration of interface elements. *Int J Numer Methods Eng*. 1993;36:43-66.
6. Ortiz M, Pandolfi A. Finite-deformation irreversible cohesive elements for three-dimensional crack-propagation analysis. *Int J Numer Methods Eng*. 1999;44:1267-1282.
7. Parrinello F, Failla B, Borino G. Cohesive-frictional interface constitutive model. *Int J Solids Struct*. 2009;46:2680-2692.
8. Paggi M, Wriggers P. Node-to-segment and node-to-surface interface finite elements for fracture mechanics. *Comput Methods Appl Mech Eng*. 2016;300:540-560.
9. Chen L, Lingen FJ, de Borst R. Adaptive hierarchical refinement of NURBS in cohesive fracture analysis. *Int J Numer Methods Eng*. 2017;112:2151-2173.
10. Paggi M, Reinoso J. A variational approach with embedded roughness for adhesive contact problems. *Mech Adv Mater Struct*. 2020;27:1731-1747.
11. de Borst R, Gutiérrez MA. A unified framework for concrete damage and fracture models including size effects. *Int J Fract*. 1999;95:261-277.
12. Reinoso J, Paggi M, Blázquez A. A nonlinear finite thickness cohesive interface element for modeling delamination in fibre-reinforced composite laminates. *Compos Part B Eng*. 2017;109:116-128.
13. Paggi M, Wriggers P. A nonlocal cohesive zone model for finite thickness interfaces–part i: mathematical formulation and validation with molecular dynamics. *Comput Mater Sci*. 2011;50:1625-1633.
14. Miehe C, Hofacker M, Welschinger F. A phase field model for rate-independent crack propagation: robust algorithmic implementation based on operator splits. *Comput Methods Appl Mech Eng*. 2010;199:2765-2778.
15. Bourdin B, Francfort GA, Marigo JJ. Numerical experiments in revisited brittle fracture. *J Mech Phys Solids*. 2000;48:797-826.
16. Borden MJ, Verhoosel CV, Scott MA, Hughes TJR, Landis CM. A phase-field description of dynamic brittle fracture. *Comput Methods Appl Mech Eng*. 2012;217-220:77-95.
17. Francfort GA, Marigo JJ. Revisiting brittle fracture as an energy minimization problem. *J Mech Phys Solids*. 1998;46:1319-1342.
18. Wu JY. A unified phase-field theory for the mechanics of damage and quasi-brittle failure. *J Mech Phys Solids*. 2017;103:72-99.
19. Verhoosel CV, de Borst R. A phase-field model for cohesive fracture. *Int J Numer Methods Eng*. 2013;96:43-62.
20. Bourdin B, Francfort GA, Marigo JJ. The variational approach to fracture. *J Elast*. 2008;91:5-148.
21. Vignollet J, May S, de Borst R, Verhoosel CV. Phase-field models for brittle and cohesive fracture. *Meccanica*. 2014;49:2587-2601.
22. May S, Vignollet J, de Borst R. A numerical assessment of phase-field models for brittle and cohesive fracture: Γ-convergence and stress oscillations. *Eur J Mech A/Solids*. 2015;52:72-84.
23. Ghaffari Motlagh Y, de Borst R. Considerations on a phase-field model for adhesive fracture. *Int J Numer Methods Eng*. 2020;121:2946-2963.
24. Chen L, de Borst R. Phase-field regularised cohesive zone model for interface modelling. *Theor Appl Fract Mech*. 2022;103:630.
25. Nguyen TT, Yvonnet J, Zhu QZ, Bornert M, Chateau C. A phase-field method for computational modeling of interfacial damage interacting with crack propagation in realistic microstructures obtained by microtomography. *Comput Methods Appl Mech Eng*. 2016;312:567-595.
26. Conti S, Focardi M, Iurlano F. Phase field approximation of cohesive fracture models. *Anna Ins Henri Poin C Anal Nonlinéaire*. 2016;33:1033-1067.
27. Chen L, de Borst R. Phase-field modelling of cohesive fracture. *Eur J Mech A/Solids*. 2021;90(104):343.
28. Feng Y, Fan J, Li J. Endowing explicit cohesive laws to the phase-field fracture theory. *J Mech Phys Solids*. 2021;152(104):464.

29. Bourdin B, Chukwudozie C, Yoshioka K. *A Variational Approach to the Numerical Simulation of Hydraulic Fracturing*. SPE annual technical conference and exhibition; 2012.
30. Chen L, Wang Z, Li B, de Borst R. Computation of the crack opening displacement in the phase-field model. *Int J Solids Struct*. 2023;283(112):496.
31. Chukwudozie C, Bourdin B, Yoshioka K. A variational phase-field model for hydraulic fracturing in porous media. *Comput Methods Appl Mech Eng*. 2019;347:957-982.
32. Yoshioka K, Naumov D, Kolditz O. On crack opening computation in variational phase-field models for fracture. *Comput Methods Appl Mech Eng*. 2020;369(113):210.
33. Paggi M, Reinoso J. Revisiting the problem of a crack impinging on an interface: a modeling framework for the interaction between the phase field approach for brittle fracture and the interface cohesive zone model. *Comput Methods Appl Mech Eng*. 2017;321:145-172.
34. Fantoni F, Bacigalupo A, Paggi M, Reinoso J. A phase field approach for damage propagation in periodic microstructured materials. *Int J Fract*. 2020;223:53-76.
35. Zhang P, Feng Y, Bui TQ, Hu X, Yao W. Modelling distinct failure mechanisms in composite materials by a combined phase field method. *Compos Struct*. 2020;232(111):551.
36. Bian PL, Qing H, Schmauder S. A novel phase-field based cohesive zone model for modeling interfacial failure in composites. *Int J Numer Methods Eng*. 2021;122:7054-7077.
37. Tan W, Martinez-Paneda E. Phase field predictions of microscopic fracture and r-curve behaviour of fibre-reinforced composites. *Compos Sci Technol*. 2021;202(108):539.
38. Hu Z, Suo X, Wang M, Jiang F, Huang H, Shen Y. A phase-field-cohesive-zone framework to simulate multiple failure mechanisms of elastoplastic fiber-reinforced composites. *Int J Fract*. 2023;1–17.
39. Dugdale DS. Yielding of steel sheets containing slits. *J Mech Phys Solids*. 1960;8:100-104.
40. Barenblatt GI. The mathematical theory of equilibrium cracks in brittle fracture. *Adv Appl Mech*. 1962;7:55-129.
41. Xu XP, Needleman A. Void nucleation by inclusion debonding in a crystal matrix. *Model Simul Mater Sci Eng*. 1993;1:111-132.
42. Chen L, de Borst R. Cohesive fracture analysis using Powell-Sabin B-splines. *Int J Numer Anal Methods Geomech*. 2019;43:625-640.
43. García I, Paggi M, Mantič V. Fiber-size effects on the onset of fiber-matrix debonding under transverse tension: a comparison between cohesive zone and finite fracture mechanics models. *Eng Fract Mech*. 2014;115:96-110.
44. Guillén-Hernández T, García I, Reinoso J, Paggi M. A micromechanical analysis of inter-fiber failure in long reinforced composites based on the phase field approach of fracture combined with the cohesive zone model. *Int J Fract*. 2019;220:181-203.
45. Pranavi D, Rajagopal A, Reddy JN. Interaction of anisotropic crack phase field with interface cohesive zone model for fiber reinforced composites. *Compos Struct*. 2021;270(114):38.
46. Li G, Yin BB, Zhang LW, Liew KM. Modeling microfracture evolution in heterogeneous composites: a coupled cohesive phase-field model. *J Mech Phys Solids*. 2020;142(103):968.
47. Chen L, Li B, de Borst R. The use of Powell-Sabin B-splines in a higher-order phase-field model for crack kinking. *Comput Mech*. 2021;67:127-137.
48. Chen L, Li B, de Borst R. Energy conservation during remeshing in the analysis of dynamic fracture. *Int J Numer Methods Eng*. 2019;120:433-446.

How to cite this article: de Borst R, Chen L. Phase-field modelling of cohesive interface failure. *Int J Numer Methods Eng*. 2023;e7412. doi: 10.1002/nme.7412